Sequence-Dependent Self-Coacervation in High Charge-Density Polyampholytes

Journal:	*Molecular Systems Design & Engineering*
Manuscript ID	ME-ART-06-2019-000074.R1
Article Type:	Paper
Date Submitted by the Author:	31-Jul-2019
Complete List of Authors:	Madinya, Jason; University of Illinois at Urbana-Champaign, Department of Chemical and Biomolecular Engineering Chang, Li-Wei; University of Massachusetts Amherst, Department of Chemical Engineering Perry, Sarah; University of Massachusetts Amherst, Department of Chemical Engineering Sing, Charles; University of Illinois at Urbana-Champaign, Department of Chemical and Biomolecular Engineering

Design, System, and Application Statement

This paper uses a combination of a simulation-informed theory and experiments to probe the monomer-level interactions that give rise to phase separation in polyampholyte solutions. More specifically, both the theoretical model and experiments were designed to understand how charge-driven liquid-liquid phase separation – a process known as *self-coacervation* can be designed by tuning the patterning of charged monomers. This molecular-level design scheme is inspired by the role of sequence in intrinsically disordered proteins, which form membrane-less organelles that play a key biological role in intracellular compartmentalization and biomolecular sequestration. Sequence-defined polyampholytes represent a model system that can undergo similar phase separation, and have implications for the development of bio-inspired materials for a variety of applications such as protein stabilization, drug-delivery, and cell signaling and regulation. Our computational model and experimental results provide insight into how to design bio-inspired soft materials using by engineering the specific sequence of charged monomers.

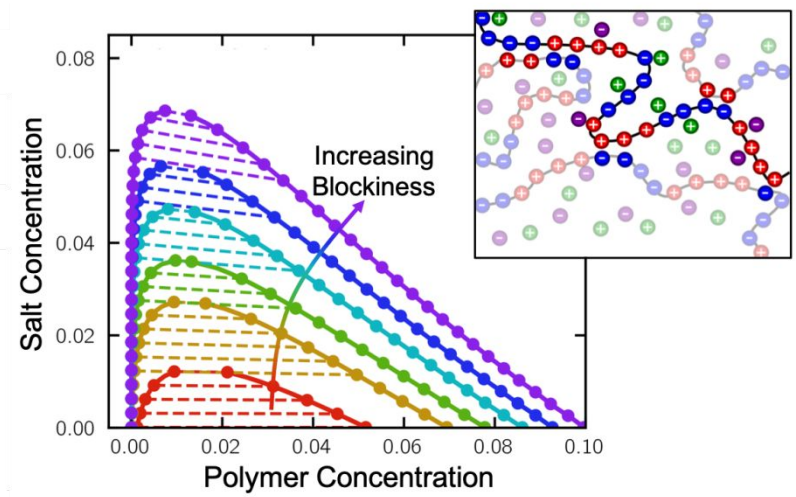

Experiment and theory show how charge monomer sequence can be used to control self-coacervation in blocky polyampholytes.

Journal Name

ARTICLE TYPE

Cite this: DOI: 00.0000/xxxxxxxxxx

Sequence-Dependent Self-Coacervation in High Charge-Density Polyampholytes†

Jason J. Madinya,[‡*] Li-Wei Chang,[◇*] Sarah L. Perry,[◇b] and Charles E. Sing[‡a]

Received Date
Accepted Date

DOI: 00.0000/xxxxxxxxxx

Polyampholytes, which contain both positive and negative charges along the backbone, represent a classical model system for certain types of 'intrinsically-disordered proteins' (IDPs). IDPs can possess biological functionality, even in an unfolded state, including the formation of phase-separated regions within a cell; while driven by a number of interactions, electrostatic attractions are thought to be key to forming these structures. This process of electrostatically-driven liquid-liquid phase separation, known as 'complex coacervation', can also be observed in simpler polymer or biopolymer systems. In this paper, we use a series of model polyampholytic polypeptides of increasing blockiness, that undergo 'self-coacervation' due to charge attraction between polycation and polyanion blocks along the same polymer chain. We show that these polypeptides undergo complex coacervation when sequences have at least 8-12 adjacent like-charges, with increasing blockiness leading to a larger two-phase region. We simultaneously develop a theory built on the transfer-matrix formalism developed by the authors, to show how blockiness increases the strength of electrostatic interactions and subsequently promote phase separation. We explore a tradeoff that emerges due to the presence of 'charge-pattern interfaces' where the sequence of polyampholyte charges switches sign, and how these contrast with chain-ends in equivalent homopolyelectrolyte coacervates.

1 Introduction

Intrinsically disordered proteins (IDPs) are proteins that do not spontaneously fold into stable structures.[1,2] IDPs can take on a number of metastable conformations in solution, ranging from stretched coils to collapsed globules.[3] This is in contrast to globular proteins, which fold into relatively ordered structured states that correspond to their specific biological function.[4,5] This folding process proceeds from a random coiled state to the native folded structure through a kinetic 'protein folding funnel',[6] where the final folded structure represents a global free energy minimum state that is governed by the specific peptide sequence.[7] IDP peptide sequences differ from their globular counterparts in that they tend to have fewer hydrophobic residues and have a higher proportion of charged and polar groups.[2,8] Many IDPs contain both positive and negative charged residues and at least 75% of IDPs are polyampholytes.[9] IDPs can become biologically active by interacting with a 'folding partner' to produce an ordered state,[10–12] but may also interact with other proteins to yield a disordered or partially-disordered - yet still fully functional - state. These latter interactions are typically referred to as 'fuzzy' interactions.[13–16] Nevertheless, while IDPs are characterized by their disordered native structures, the distributions of the conformations sampled are not random and are governed in part by net charge,[17,18] and charge sequence.[9] This combination of conformational flexibility and diversity of interaction modes make IDPs particularly suitable for cell signaling and regulatory functions.[19–24]

Recently, there has been great interest in understanding the critical role IDPs play in the formation of membraneless organelles through a liquid-liquid phase separation process.[24–26,26–45] The solution properties that lead to solution demixing in IDPs are encoded within the sequence of the protein.[9,32,46,47] Post-translational modifications can also lead to phase separation in IDPs, for instance phosphorylation of residues along the polypeptide chain can change the electrostatic interactions leading to demixing.[30,48] It is clear that electrostatic interactions and polypeptide sequence together figure prominently in the solution behavior of IDPs. The challenge in trying to understand IDP solution behavior, and ultimately their function, is to include the the complex diversity of interactions and sequence

‡ *Department of Chemical and Biomolecular Engineering, University of Illinois at Urbana Champaign, 600 S. Matthews Ave., Urbana, IL, USA*
Email: cesing@illinois.edu
◇ *Department of Chemical Engineering, University of Massachusetts Amherst, 686 North Pleasant St., Amherst, MA, USA*
* *These authors contributed equally to this work.*
[a] *Email: cesing@illinois.edu*
[b] *Email: perrys@engin.umass.edu*

effects into macromolecular models.

One common approach to understanding IDPs has been to study the physical properties of analogous, model polymer systems. Polyampholytes, which are polymers containing both positive and negative charges, are particularly useful in this role due to the abundance of charged amino acids in IDPs. Polyampholyte models have long been considered in the polymer physics literature, with early work by Higgs and Joanny,[49] combining Debye-Hückel and scaling theory to develop an analytical model. Even here, the definition of the monomer sequence was a key attribute, with this case being a random distribution of negative and positive charges. Systematic study of this distribution by Dobrynin and Rubenstein[50] included a charge asymmetry parameter and an effective temperature in a Flory-type theory.

The distribution of charge sequence has taken center stage in the IDP literature, where IDP conformation can be described using a *sequence charge decoration* (SCD) metric[51,52] that captures the blockiness of charge. Coarse-grained simulations have been used to show connections between this SCD and single-molecule properties such as the conformational size and coil-globule transition,[53–56] and bulk phase behavior.[57–59] Similarly, recent use of *random phase approximation* (RPA) theory to describe polyampholyte bulk phase behavior has demonstrated that the propensity to undergo phase separation is correlated with the 'blockiness' of the charge pattern.[60,61] This has recently been extended by efforts from Danielsen, *et al.*[62] to use field-theoretic simulations capable of describing phase-separation in blocky polyampholytes. Indeed, this work is built on the key observation that polyampholyte phase separation is essentially equivalent to the associative phase separation between two separate, oppositely-charged polymers, a process known as *polymer complex coacervation*.[62–65] Inspired by this connection, polyampholyte phase separation is sometimes called *self-coacervation*.[62,63]

Complex coacervation itself has also been used as a polymer analogy to IDP-based phase separation in biological systems;[33] indeed, the physical understanding of coacervate physics developed by the community has striking similarities to the development of polyampholyte physics. The earliest work in this area combined Flory-Huggins theory of polymer mixing with the Debye-Hückel theory of dilute electrolytes,[66] resulting in the *Voorn-Overbeek* model.[67,68] While this theory can be fit to experimental data, it has provided the starting point for a class of field theory models[63,69–75] that seek to shore up its known limitations.[76–79] Initial efforts to use RPA-based methods were able to predict the same general phase behaviors, whilst including the connectivity between charges along a polymer chain.[72–75] These are analogous to efforts for polyampholyte systems, and culminated in the development of field-theoretic models that have now been applied to both polyampholyte and coacervate phase separation.[60–65] Similar to the development of polyampholyte physics, molecular simulation has played a key role in developing a physical understanding; this is true both at the limit of dilute *polyelectrolyte complexes* between two chains, as well as for bulk phase separation.[80–85]

Recent work on complex coacervation, inspired in part by the relevance to IDPs, has seen the emergence of a number of modeling approaches beyond the continuing efforts in using simulation and field theory. These have sought to further examine and account for the limitations present in many of the field theoretic approaches, and particularly the original Voorn-Overbeek theory.[67] For example, liquid-state theory models have incorporated the effects of both connectivity and the excluded volume of the molecular species.[86–88] Scaling models have also been developed to detail the effects of charge density and connectivity in the limit of low-charge-density.[89–92] Another class of models has recently shown promise, built on physical charge condensation arguments; here, coacervation is driven by the release of salt ions that localize near isolated polyelectrolytes, but are 'released' when charge neutralization can occur through interactions with an oppositely-charged polyelectrolyte chain instead.[93] This class of models has a number of manifestations, including a semi-phenomenological 'ion equilibrium' model used by Larson and Qin[94] and a ladder conformation-based model developed by Muthukumar.[95]

We have recently developed a model inspired by the concept of charge condensation, that we call the transfer matrix (TM) theory of coacervation.[96–100] This theory accounts for the localization of oppositely-charged small molecule ions or polyelectrolytes near a test polyelectrolyte chain, and maps this localization to a 1-D adsorption model. This versatile model has provided insights into how coacervation is affected by a number of molecular features, including charge spacing,[96] polymer stiffness and architecture,[97,100] and salt valency[97] as well as how charged block-copolymers can self-assemble via coacervation.[101] Recently, we have demonstrated that this model can be extended in a hybrid simulation/theory scheme to *arbitrary* monomer sequences for one of the polyelectrolytes.[99] The effect of charged monomer sequence on coacervation predicted by this theory is consistent both with molecular simulation and results from experiment.[99]

With the exception of field theoretic and scaling models,[60–65,89–92] most of the recent insights into coacervation have yet to be applied to self-coacervation. In part, this is complicated by the key role that sequence plays in self-coacervation, which may not be resolved by many of the coacervate models. With the advent of the sequence-dependent model in the transfer matrix theory,[99] there is now an opportunity to develop a new theory of polyampholyte self-coacervation that specifically takes into account the effect of sequence. In this paper, we extend the transfer matrix theory to consider the effect of sequence on self-coacervation, and compare to experimental trends that demonstrate the presence of a critical charge 'blockiness' where coacervation begins to be observed. The trends we observe are largely consistent with the simulation efforts by Danielsen, *et al.*,[62,102] however our alternative approach[96] is specifically designed to consider high charge-density polyelectrolytes; this limit is challenging to resolve in the field theoretic approach, due to the assumption of Gaussian-smeared charges and excluded volume that does not resolve the local charge correlations (that give rise to e.g. counterion condensation and ion pairing) important for modeling high charge-density polyelectrolyte systems.[62] Additionally, we demonstrate that our theoretical predictions match qualitatively with the observations from experiments on a set of model sequence-controlled polypeptides. Our results have impli-

cations for the phase behavior of IDPs, showing that the sequence of charges in these biomacromolecules, along with environmental parameters such as salt concentration, can strongly impact phase behavior. This could also have general implications for electrostatic interactions between globule species, such as proteins or micelles. More fundamentally, we demonstrate via experiment and simulation-informed theory how electrostatics (and specifically charge patchiness) gives rise to polymer phase separation.

2 Computational Methods

2.1 Transfer Matrix Theory

Our previous work on coarse-grained simulation models of polyelectrolyte coacervation has shown that correlations between the charged species in the coacervate phase are short-ranged.[103] This observation suggests that the thermodynamics of coacervation can be effectively captured by considering only the nearest neighbors of a test polyelectrolyte chain. This led to the development of the transfer matrix theory of coacervation.[96] Here we apply this model for polyampholyte self-coacervation. We consider a test polyampholyte chain in the presence of charged ions and other polyampholyte chains. We approximate the interactions between the particles as a 1-D adsorption model in which the monomers along the test chain are the adsorption sites onto which the oppositely-charged ion or monomers can adsorb to (Figure 1). This results in the following expression for the free energy of coacervation:

$$\frac{\mathscr{F}}{Vk_BT} = \sum_i \frac{\phi_i}{N_i}\ln\phi_i + \frac{\phi_p}{2N_p}\ln\left[\psi_0^T\mathbf{M}_0^{N_p}\psi_1\right] + \\ +\zeta\left(\sum_{i\neq W}\Lambda_i\phi_i\right)^3 + \sum_{ij}\chi_{ij}\phi_i\phi_j \qquad (1)$$

The first term of this expression is the translational entropy of all the species $i = P,S,W$ (representing the polyampholyte, salt, and water respectively) with degree of polymerization N_i. In this work, only the polymeric (i.e., the block polyampholyte and homopolyelectrolyte) species have $N_i > 1$. The second to last term is a phenomenological cubic term to capture the non-pairwise excluded volume with a magnitude governed by the parameter $\zeta = 19.0$, which is constant for this paper and parameterized based on previous simulation results.[96] The final term is the standard Flory χ term, accounting for short-range, non-electrostatic interactions. In this paper, only the polymer and solvent interact via this Flory term with prefactor χ_{pw}; for most of the paper the value of χ_{pw} is set to zero unless explicitly stated. The prefactor Λ_i accounts for differences in per-molecule excluded volumes, and is set to $\Lambda = 0.6785$, as justified in previous works.[96,99]

The second term is the interaction free energy of the polyampholyte, and the primary result of the transfer matrix theory. This interaction free energy is derived from the grand canonical partition function, Ξ^{int}, for the polyampholyte chain interacting with its local environment. This partition function is expressed using the transfer matrix formalism, $\Xi^{int} = \left[\psi_0^T\mathbf{M}_0^{N_p}\psi_1\right]$, where $\mathbf{M}_0$ is the transfer matrix that accounts for the incremental contribution to the partition function for growing a polyampholyte chain by a single monomer. This matrix contains the Boltzmann factors for the various possible adsorption states given the previous adsorption state. We denote an adsorbed salt ion as C, an adsorbed polyampholyte monomer as P and a empty adsorption side as 0. We must also distinguish between the initial monomer of a polyampholyte chain P', and subsequent monomers of that adsorbed polyampholyte chain P. For instance $C0$ denotes a state in which the current monomer has a salt ion adsorbed, and the previous monomer has no adsorbed species.The form of the transfer matrix is as follows:

$$\mathbf{M_0} = \begin{bmatrix} CC & CP & CP' & C0 \\ PC & PP & PP' & P0 \\ P'C & P'P & P'P' & P'0 \\ 0C & 0P & 0P' & 00 \end{bmatrix} \\ = \begin{bmatrix} A_0\phi_s & A_0\phi_s & A_0\phi_s & A_0\phi_s \\ 0 & F & G & 0 \\ B_0\phi_p & B_0\phi_p & B_0\phi_p & B_0\phi_p \\ D & D & D & D \end{bmatrix} \qquad (2)$$

The Boltzmann factor for having a salt ion adsorb is written as in previous work as $A_0\phi_s$, and similarly the Boltzmann factor for having the initial monomer of polyampholyte chain adsorb is set to $B_0\phi_p$. The prefactors for these Boltzmann factors were previously parameterized to match coarse-grained simulation when $A_0 = 20.5$ and $B_0 = 12.2$.[96] We assign an electrostatic energy penalty to charged monomers that are un-paired $\varepsilon(s)$, which is dependent on the monomer index s. This is used in the quantity $D = e^{\varepsilon(s)}$. Finally, the Boltzmann factors for the case of having a subsequent monomer following a newly adsorbed chain and a previously adsorbed chain, G and F respectively, depend on the probability of the current monomer along the adsorbed chain being the counter-ion to the current monomer of the test chain. The vector $\psi_1 = [C,P,P',0]^T = \left[A_0\phi_s, 0, B_0\phi_p, e^{\varepsilon(0)}\right]^T$ is comprised of the Boltzmann factors for the first monomer along the chain. The vector ψ_0 is a vector of all ones.

In this transfer matrix theory, the charge sequence effects are manifested in the Boltzmann factors D, F and G. For this work, we will consider polyampholytes with zero net charge that are comprised of alternating blocks of opposite charge and equal size. In this case, the charge pattern of the chain can be described by a single value, τ, that represents the length of one repeat unit comprised of one polycation block followed by one polyanion block. The form of the Boltzmann factors F and G depends on whether or not the specified monomer along the chain is at a charge-sign interface, meaning it is followed by a monomer of the opposite charge. For monomers away from the charge-sign interface, $F = (\tau-4)/(\tau-2)$ and $G = 2-4/\tau$. In the case of F, where two consecutive monomers on an already adsorbed chain are both adsorbed onto the test chain, the probability that they are both counter-ions to the test chain is $(\tau/2-2)/(\tau/2-1)$. For monomers at the charge-sign interface, $F = (2)/(\tau-2)^*$ and $G = 4/\tau$, with the exception in the case of $\tau = 2^*$ in which $F = 1.0$.

In the limit as $\tau \to \infty$, the values for F and G approach their respective values for a homopolyelectrolyte. This leaves the Boltzmann factor D to be determined in order to evaluate the interaction partition function for the polyampholyte chain. The electrostatic energy penalty $\varepsilon(s)$ is determined from coarse grained simulations of a test chain in a dilute salt solution.

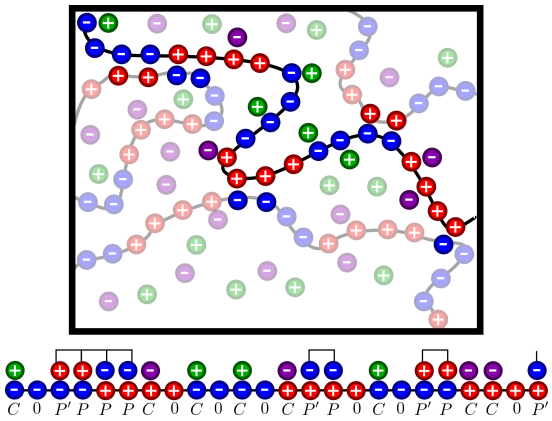

Fig. 1 Schematic illustrating the coacervate phase of a polyampholyte solution. The opaque species represent the test the chain and its nearest neighbors. The monomers along the test chain are treated as adsorbtion sites onto which salt ions or monomers from other polyampholyte chains can adsorb. Walking along the test chain, each monomer is assigned an adsorption state for salt ion C, initial adsorbed monomer from a polyampholyte chain P', a subsequent monomer from an already adsorbed polyampholyte chain P, or no adsorbed species 0. It is preferential for the adsorbed chain to be in the coacervate phase as it allows for many more configurations of adsorption states due to the higher density of charged species.

2.2 Single Polyampholyte Chain Coarse-Grained Simulations

It is electrostatically unfavorable for a charged monomer not to be paired with an oppositely-charged salt ion or polyelectrolyte, especially in the limit of high linear charge density. Previous work has shown that the localization of opposite charges along a sequenced polyelectrolyte is profoundly influenced by the sequencing of the charges along the chain,[99,104] which we expect to be especially important in the case of polyampholytes that have a combination of repulsive and attractive electrostatic interactions due to the presence of both positive and negative charges along the chain.

Previous work on sequence-defined polyelectrolytes have shown that single-chain simulations are a powerful way to inform the transfer matrix model,[99,104] allowing us to correlate the electrostatic energy penalty $\varepsilon(s)$ to monomer-specific salt ion localization. In this work, we consider a single fully extended and fixed, sequenced polyampholyte in a dilute salt solution. We note that this is subtly different from previous efforts that do not extend the polyelectrolyte chain.[99] In this work we do extend the chain to avoid self-collapse of the polyampholyte, and have verified that it does not noticeably alter the values of $\varepsilon(s)$ obtained. Monte Carlo (MC) simulations are performed for single polyampholyte chains in dilute salt solution using the restricted primitive model (Figure 2). The solvent, water, is modeled as a continuum with a relative dielectric constant $\varepsilon_r = 78.5$. Salt ions and polyampholyte monomers are modeled as charged hard spheres with a diameter $\sigma = 4.25$ Å. The total potential U is the sum of the electrostatic potential U_{ES}, and the hard-sphere potential U_{HS}.

$$U = U_{ES} + U_{HS} \tag{3}$$

The electrostatic potential is set to a Coulomb potential:

$$U_{ES} = \sum_i \sum_{j>i} \frac{q_i q_j e^2}{4\pi\varepsilon_0 \varepsilon_r r_{ij}} \tag{4}$$

where q_i is the valency of the bead i, e is the electron charge, ε_0 is the vacuum permittivity, and r_{ij} is the distance between beads i and j.The electrostatic interactions are evaluated using Ewald summation. The excluded volume of the ions and monomers are captured using a hard-sphere potential:

$$U_{HS} = \sum_i \sum_{j>i} \begin{Bmatrix} \infty & r_{ij} < & \sigma \\ 0 & r_{ij} >= & \sigma \end{Bmatrix} \tag{5}$$

Each MC simulation is run for 10×10^6 MC timesteps. The number charge densities are evaluated after an equilibration period of 1×10^6 MC timesteps by counting the number of salt ions within a cutoff separation, $r_c = 1.5\sigma$, for each monomer. These simulations were performed at salt concentration of $\phi_s = 1.32 \times 10^{-4}$.

Salt ion localization for a given monomer in the sequence is quantified from MC simulations by evaluating the ratio of the local number charge density, $n_c(s)$, and the local number charge density in the case where electrostatic interactions are turned off, $n_c^0(s)$. We can approximate $n_c(s)$ and $n_c^0(s)$ using a simple, uncorrelated adsorption model which gives the following expression:

$$n_c(s) \sim e^{-(\varepsilon'(s)-\mu)} / \left(1 + e^{-(\varepsilon'(s)-\mu)}\right)$$

$$n_c^0(s) \sim e^{\mu} / (1 + e^{\mu}) \tag{6}$$

In the dilute salt limit, such that $e^{\mu} \ll 1$, we can define an electrostatic association strength as, $\varepsilon'(s) = \ln\left(n_c(s)/n_c^0(s)\right)$. We have previously shown this quantity to be independent of the simulation salt concentration ϕ_s in the appropriate limit.[99] For a given polyampholyte sequence, we set a reference state as the average electrostatic association strength of a homopolyelectrolyte with the same degree of polymerization as the polyampholyte. Finally we set the electrostatic energy penalty in the Boltzmann factor D to be equal to the deviation of the electrostatic association energy of the polyampholyte from the reference state.

$$\varepsilon(s) = \left\langle \ln\left(\frac{n_{c,hp}(s)}{n_{c,hp}^0(s)}\right)\right\rangle - \ln\left(\frac{n_c(s)}{n_c^0(s)}\right) \tag{7}$$

To carry out this calculation for a polyampholyte, where the sequence is defined by the charge block size $\tau/2$ and the number of charge-blocks, three MC simulations are performed. The first simulation is for the sequenced polyampholyte chain, the second is for the homopolyelectrolyte with the same degree of polymerization as the polyampholyte, and the third is for a neutral chain

with the same degree of polymerization as a single charged block. All simulations were repeated 10 times, and the average $\varepsilon(s)$ was calculated.

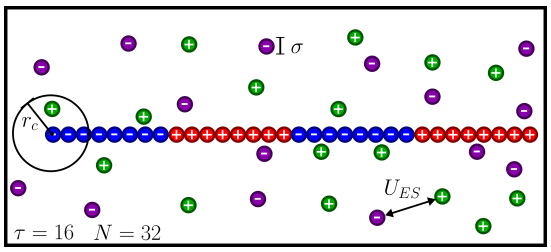

Fig. 2 Schematic illustrating the restricted primitive model Monte Carlo (MC) simulation of single polyampholyte chain. The chain is stretched and fixed, with the charges distributed according to the 'blockiness' parameter τ. The salt ions are free to translate in the simulation box according to the potential U, which comprised of a Coulombic electrostatic potential U_{ES} and a hard sphere potential U_{HS} to account for the excluded volume of the various particles. The particle diameter is given by σ and the bond length is 1.05σ.

3 Experimental Methods

3.1 Polyampholyte and Polypeptide Synthesis

A series of lysine-glutamate polyampholytes with increasing blockiness (*i.e.,* $(K_8E_8)_3$, $(K_{12}E_{12})_2$, $(K_{15}E_{15})_2$, and $K_{24}E_{24}$), along with homopolypeptides corresponding to the individual blocks (*i.e.,* K_{12}, E_{12}, K_{15}, E_{15}). Both polyampholytes and homopolypeptides were prepared using standard Fmoc-based solid-phase synthesis[105] on a Liberty Blue automated microwave peptide synthesizer from CEM, Ltd. using methods reported previously.[99,104] Briefly, synthesis of polyampholytes and homopolypeptides was performed on low loading Rink amide Protide resin (0.19 mmol/g, CEM) and Rink amide MBHA resin (0.32 mmol/g, Peptide Solutions), respectively, using Fmoc-L-Lys(Boc)-OH, Fmoc-D-Lys(Boc)-OH, Fmoc-L-Glu(tBu)-OH and Fmoc-D-Glu(tBu)-OH (Peptide Solutions, LLC). 20% Piperidine (Sigma Aldrich) in N,N-dimethylformamide (DMF, sequencing grade, Fisher BioReagents) was used for Fmoc deprotection, while 0.5 M N,N-diisopropylcarbodiimide (DIC, 99% Acros Organics) and 0.5 M ethyl (hydroxyimino)cyanoacetate (Oxyma, Peptide Solutions) in DMF were used as activator and base, respectively. Double coupling was applied to all lysine monomers in polyampholytes to increase the yield. Cleavage from the resin and side-chain deprotection was performed in 95/2.5/2.5% (v/v) trifluoroacetic acid (TFA, Fisher)/water (MilliQ 18.2 MΩ cm, Millipore)/triisopropylsilane (98% Acros Organics) for 3 hours at room temperature. The resulting peptides were precipitated into cold anhydrous ethyl ether (BHT stabilized, Fisher Scientific). The final product was characterized by matrix-assisted laser desorption/ionization time of flight mass spectrometer (MALDI-TOF, Bruker UltrafleXtreme).

All peptides were synthesized using amino acids of alternating chirality (D and L) to mitigate inter-peptide hydrogen bond formation.[106–108] Lysine groups are neutralized by a TFA counterion. Glutamate groups are neutralized by sodium.

3.2 Preparation of Stock Solutions

Polyampholyte and homopolypeptide stock solutions were prepared gravimetrically using Milli-Q water at a concentration based on the total number of amino acids present and adjusted to pH = 7.0 ± 0.03 using concentrated solutions of HCl and NaOH (Fisher Scientific), as needed. For instance, a stock solution of the homopolyanion poly(glutamate) of 10 mM amino acid would be used in parallel with a stock solution of an oppositely-charged poly(lysine), also at 10 mM with respect to the total number of amino acids. For polyampholytes, a stock solution of poly(lysine-co-glutamate) of 10 mM amino acid would consist of 5 mM lysine and 5 mM glutamate, respectively. Sodium chloride (NaCl) was purchased from Sigma Aldrich (ACS reagent). A stock solution was prepared gravimetrically at 4 M and adjusted to pH = 7.0, as above.

3.3 Coacervate Preparation and Characterization

Complexation was performed using stoichiometric quantities of positively and negatively charged polypeptides at a total charged residue concentration of 1 mM, 10 mM, 20 mM, 40 mM and 50 mM at pH 7.0. Under these conditions, it is a reasonable approximation to describe all of the residues on both polyampholytes and polypeptides as fully charged. Homopolypeptide coacervate samples were prepared by first mixing a concentrated solution of NaCl with MilliQ water in a microcentrifuge tube (1.5 mL, Eppendorf), followed by the polyanion. The resulting mixture was then vortexed for 5 s before addition of the polycation. The final mixture was vortexed for at least 15 s immediately after the addition of polycation to ensure fast mixing. For polyampholyte samples, the peptide was added directly into the water-NaCl mixture, followed by vortexing as described above. Notably, the low levels of salt allowed for phase separation in our polyampholyte stock solutions. Therefore, it was critically important to ensure that the stock solution was well mixed prior to pipetting. Phase separation could be observed via an increase in the turbidity, and/or the opalescent appearance of the samples, due to the formation of small droplets of the complex coacervate phase.

3.3.1 Determination of Salt Resistance

Samples were then examined using brightfield optical microscopy (EVOS XL Core, Fisher Scientific) to confirm the liquid nature of the droplets, and to determine the 'salt resistance,' ϕ_p^s, or the salt concentration above which no phase separation occurs. All samples were imaged within 1 h of preparation. Error bars on measurements of the salt resistance correspond to the salt concentration intervals over which samples were prepared.

3.3.2 Fourier Transform Infrared (FTIR) Spectroscopy

Attenuated total reflectance Fourier transform infrared spectrometry (ATR-FTIR, Platinum ATR, Bruker Alpha, Billerica, MA) was used to analyze the secondary structure of complexes resulting from polyampholytes and homopolypeptides. The amide I carbonyl stretching vibration were measured by FTIR (1600-1700 cm^{-1}) to detect the formation of secondary structure of peptide-based complexes. All complex samples were prepared at a total charged residue concentration 65 mM at pH = 7.0. Lyophilized

(Labconco, FreeZone Plus 2.5 Liter Cascade Console Freeze-Dry System, Kansas City, MO) complex samples then were examined by FTIR, and the resulting spectra were normalized at 1650 cm^{-1} to facilitate comparison.

4 Results and Discussion

Using the transfer matrix model, we evaluate the propensity for various sequences of model polyampholytes and their analogous homopolyelectrolytes to undergo self-coacervation or complex coacervation, respectively. The transfer matrix model is informed by Monte Carlo simulations that evaluate the sequence-dependent electrostatic association strength for each monomer along the chain. The system free energy described in Eq. 1 is minimized to resolve the two-phase coexistence boundaries and compositions as a function of 'blockiness' as well as the number of charged blocks; these results are compared to experimentally-determined salt resistances for sequenced polyampholtyic polypeptides and homopolypeptides.

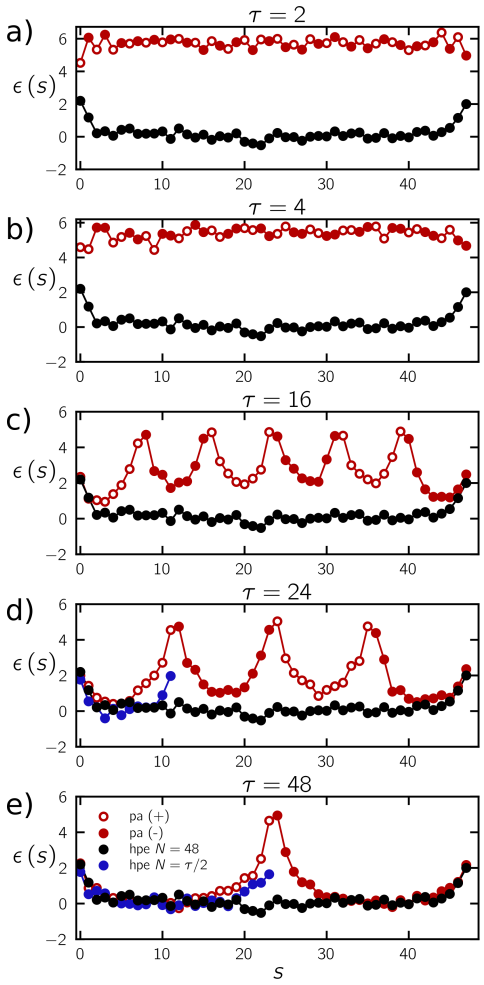

Fig. 3 Monomer-dependent energy $\varepsilon(s)$ as a function of chain index, calculated from Eq. 7 using MC simulations for polyampholytes (pa, red) of increasing 'blockiness' τ. Open points are for the cation (+) beads and the filled points are for the anion (–) beads. These data are compared with a full-length homopolyelectrolyte (hpe, black) where $N_p = 48$. For $\tau = 24$ and $\tau = 48$, results are also shown for homopolyelectrolytes where $N_p = \tau/2$ (blue).

4.1 Salt Ion Localization From MC Simulations

In our transfer matrix theory, electrostatic sequence effects are described by the electrostatic energy parameter $\varepsilon(s)$, as determined from single chain MC simulations. Therefore, we study the trends in this parameter as a function of sequence 'blockiness' τ. The polyampholyte sequences are characterized by the 'blockiness' τ as well as the number of charged-blocks in the chain. In Figure 3, we show how the charge sequence affects salt ion localization around the chain by plotting $\varepsilon(s)$ for a polyampholyte chain with a degree of polymerization $N_p = 48$, and a homopolyelectrolyte with the same degree of polymerization. The homopolyelectrolyte exhibits a near-constant value of $\varepsilon(s) \approx 0$ along the center of the chain, which reflects the normalization condition in Eq. 7. Deviations only occur at the chain ends, suggesting that except for the 2-4 monomers at the chain end, the electrostatic environment around most homopolyelectrolyte monomers is similar to that of an infinite line of charge. This reflects a significant localization of the oppositely-charged salt ions near the polyelectrolyte chain. At the chain ends, there is a marked increase in $\varepsilon(s)$ that reflects the transition from appearing as an 'infinite' line of charge to a 'semi-infinite' line of charge. Here, the last monomer of the chain does not get the 'advantage' of like-charged monomers connected on both sides, in terms of localizing the opposite charge, therefore it is less likely to have salt ions condensed near the chain-ends.

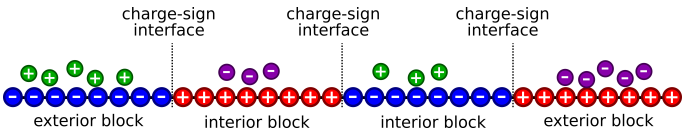

Fig. 4 Schematic of salt localization along polyampholyte chains with $\tau = 16$. The key features are the chain ends and the charge-sign interfaces. Both chain ends and charge-sign interfaces reduce salt localization however the charge-sign interfaces sees even more reduction in salt localization.

Analysis of our polyampholyte systems demonstrates that the pattern of positive and negative charges strongly affects charge confinement. This is apparent as the blockiness τ of the charge patterns increases from alternating positive-negative monomers ($\tau = 2$) to blocks of 24 positive and negative monomers ($\tau = 48$), seen in Figure 3. Here, the key difference is the presence of *charge-patterning interfaces* where the sign of the sequence changes from positive to negative (Figure 4). For $\tau = 2$, this occurs every monomer. Correspondingly, the value of the electrostatic energy parameter $\varepsilon(s) \approx 6$ reflects the weak localization of salt charges near to the polyampholyte, meaning that the opposite charges of the residue can effectively neutralize each other without the need for additional salt ions. Due to this close proximity of positive and negative charges, we observed an increase in salt ion localization (*i.e.,* lower values of $\varepsilon(s)$) at the chain ends where there are fewer nearby, opposite charges. Modest increases in the blockiness do not lead to large changes in the electrostatic environment, shown by $\tau = 4$.

As blockiness increases significantly, for example to $\tau = 16$, salt ions become increasingly localized by the long runs of positive

and negative monomers. The charge-patterning interface, located every 8 monomers, is quantitatively similar in $\varepsilon(s)$ to the $\tau = 2$ case and does not significantly localize salt ions near the polyampholyte chain. Nevertheless, as these charge-patterning interfaces become less frequent along the polyampholyte sequence, the regions in between become closer to the homopolyelectrolyte limit of $\varepsilon(s) \to 0$. This is observed as τ is increased from 24 to 48.

We further demonstrate the significance of these charge-patterning interfaces by comparing the values of $\varepsilon(s)$ for a polyampholyte with large τ to those for homopolymers with the same degree of polymerization as the component blocks (*i.e.* $N_P = \tau/2$) in Figure 3a and Figure 3e. The homopolymer values for ε are shown as blue dots. Deviations between the values of ε are most significant when comparing the chain ends of the homopolyelectrolyte and the location of the charge-patterning interface ($s = 10, 11$ for $\tau = 24$ and $s = 22, 23$ for $\tau = 48$). Here, salt ion localization is significantly stronger for chain-ends than for the charge-patterning interface, which we attribute to the presence of the nearby oppositely-charged monomers (Figure 4).

4.2 Phase Behavior Predicted By Transfer Matrix Theory Model

The electrostatic energy parameters $\varepsilon(s)$ determined from the MC simulations are used to evaluate the polyampholyte chain partition function and subsequently the system free energy Eq. 1. We plot the resulting phase diagrams in Figure 5 for the sequenced tetra-block polyampholytes, as well as their analogous homopolyelectrolyte where $N_p = \tau/2$. In these phase diagrams, the binodal curves demarcate a region of salt-polymer concentrations (ϕ_s versus ϕ_p) within which phase separation occurs. Two 'branches' of the binodal at high and low polymer concentrations ϕ_p are connected by tie-lines denoting the two values of ϕ_p and ϕ_s that are in coexistence. Similar to prior results for both simulation and experiments on homopolyelectrolyte coacervates,[96,103] these tie-lines exhibit negative slopes indicating that the polymer-dense coacervate phase (high ϕ_p) has a lower salt concentration than the polymer-dilute supernatant phase (low ϕ_s). For this transfer matrix model for coacervation, this salt partitioning to the supernatant phase has been attributed to the high excluded volume in the coacervate phase.[86,96–98,103] This is consistent with other theoretical results,[73,74,86,95] and is supported by experiment and simulations.[103,109–112] The negative slope of the tie line distinguishes this model from theories accurate in the low-charge density limit, which exhibit tie lines with negligible or positive slopes.[62,63,67,72] Here, salt partitioning is driven by the increased electrostatic attractions in the charge-dense (i.e., polymer dense) phase.[62,63,67,72,113,114]

Figure 5 highlights the difference between polyampholyte and homopolyelectrolyte coacervation, with comparable values of τ and N_p such that the main molecular difference is that the homopolyelectrolytes can be 'connected' to yield the blocky polyampholytes. A few key trends are apparent in this set of phase diagrams. We observe an increase in the size of the two-phase region that is consistent with the increased salt ion localization along the stretched polyampholytes in Figure 3 as a function of increasing

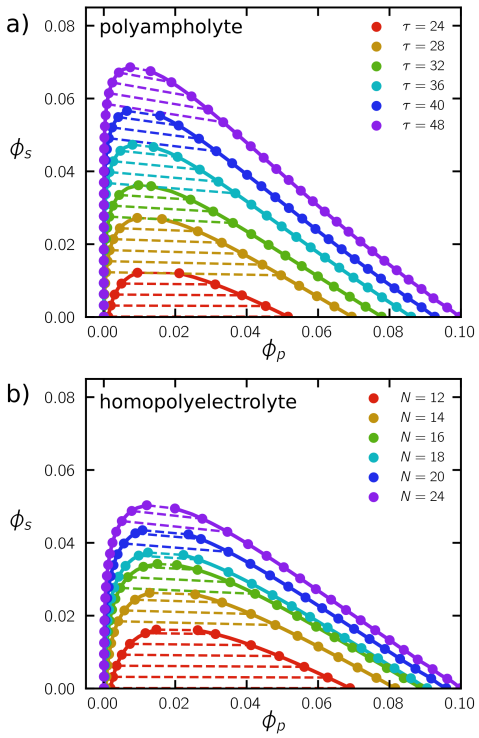

Fig. 5 Plots showing the phase diagrams for polyampholytes (a), and their analogous homopolyelectrolytes (b) for varying values for τ. The homopolyelectrolyte degree of polymerization is set to be $N_p = \tau/2$ The dotted lines represent the tie lines for the two phases. The tie lines are shown for each curve where the lower τ value tie lines are shown when the coexistence regions of overlaps with the coexistence region of another τ curve.

τ, and thus an increase in the entropic driving force. This also correlates with the decrease in regions along the polyelectrolyte chain affected by the charge-pattern interfaces, where the switch from positive to negative charges in the monomer sequence prevents charge localization and thus weakens the electrostatic driving force for coacervation. This sequence effect persists even for block sizes as large as $\tau = 48$, which we attribute to the effect that a single charge-patterning interface has on values of $\varepsilon(s)$ as far as 10 monomers away along the chain contour. A similar trend is observable in the homopolyelectrolytes, where an increase in chain length corresponds to an increase in the two-phase region. Here, there are no charge-pattern interfaces, and instead the weaker salt localization at the chain ends plays a similar role in weakening phase separation at lower values of N_p that have a higher fraction of chain ends.

In addition to the presence of charge-pattern interfaces or chain ends, both polyampholyte and homopolyelectrolyte coacervation are expected to be affected by differences in the translational entropy of the polymeric species. Larger N_p and larger τ represent larger chains, and thus there is an increase in the number of polyelectrolyte charged interactions per chains. This chain-length effect has long been understood to play a role in homopolyelectrolyte coacervation,[115] and we expect it to complement charge-sequence effects here.

Figure 6 provides a summary of the simulation results, plotted

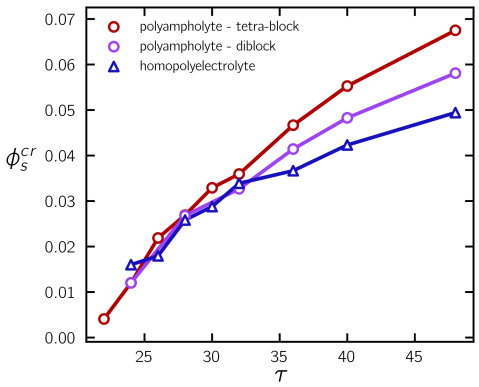

Fig. 6 Plots of the critical salt concentrations for the tetra-block polyampholyte (red), the di-block polyampholyte (magenta), and their analogous homopolyelectrolyte (blue) as a function of τ. For the homopolyelectrolyte, $\tau = 2N$.The dashed lines are to guide the eye.

as the critical salt concentration ϕ_s^{cr} as a function of the blockiness τ (for polyampholytes) and $2N_p$ (for homopolyelectrolytes). The value ϕ_s^{cr} is simply the maximum salt concentration ϕ_s where phase separation can be observed. This allows for the direct comparison of the phase diagrams in Figure 5, which exhibit an increase in the two-phase region with both increasing τ or N_p. We show that, at large values of $\tau > 32$, the strength of phase separation increases with increasing chain length; the homopolyelectrolyte for $N_p = 24$, for example, corresponds to a di-block polyampholyte of $\tau = 48$, which has a chain length of $N_p = 48$. Extending this polymer to consider a tetra-block polyampholyte with a chain length of $N_p = 96$, we observe a commensurate increase of ϕ_s^{cr} that we attribute primarily to the increase in charges per single-chain translational degree of freedom.

In contrast, at low values of $\tau \leq 32$, we observe similar values of ϕ_s^{cr} for the three different types of coacervates. We attribute this to a tradeoff between the number of charges per chain, and the differences between the strength of charge localization at chain ends versus charge-pattern interfaces. These effects cancel out, because as the number of charges per chain increases (homopolyelectrolyte to di-block polyampholyte to tetra-block polyampholyte), the chain ends are also replaced by charge-pattern interfaces that are weaker at localizing charges.

To demonstrate how this cancellation of sequence effects occurs, we show in Figure 7 a series of di-block versus tetra-block polyampholytes as the value of τ is increased. We note that this shows the transition out of the cancellation regime and into the regime where the two polyampholyte types significantly deviate. We highlight two trends; with increasing τ, the higher values of N_p (the tetra-blocks) are more sharply peaked near the critical point, reflecting the approach of the critical point to smaller values of ϕ_P at larger values of N_p. However, there is a second trend of the value of ϕ_P at $\phi_s = 0$, where the tetra-block binodal is initially at *lower* values of ϕ_P than the di-block, however this inverts at larger values of τ. This inversion occurs because, in traditional polymer-solvent phase diagrams, the binodal moves to larger values of ϕ_P for larger values of N_p. This is the case at large τ. However, at lower values of τ the phase separation is weaker for the tetra-block due to the presence of more charge-pattern interfaces.

4.3 Comparison of Experimental, Theoretical Observations in Polyampholyte Self-Coacervation

The trends predicted by our transfer matrix theory show good qualitative agreement with experimental observations. In particular, we compare how the salt resistance ϕ_s changes as a function of polymer concentration ϕ_p, for polyampholytes and their analogous homopolyelectrolyte coacervates Both theory (Figure 8a) and experiment (Figure 8b) exhibit a significant decrease in salt resistance as the polymer concentration decreases. The trends in salt resistance also increase with increasing block size τ or chain length N. Additionally, the salt resistance is higher for the di-block polyampholyte than for the analogous 'split' component homopolyelectrolytes.

In these comparisons, we note that the theoretical results included a value of the χ_{pw}-parameter ($\chi_{pw} = 0.25$) to account for short-range interactions, parameterized to compare well with experimental data; nevertheless, the trends are consistent regardless of this choice. We note that we generally do not expect quantitative matching, as this theory invokes a mean-field approximation in the transfer matrix calculation that is not accurate at low ϕ_p. Furthermore, the coarse-grained representation we use does not resolve physical phenomena at the atomistic level, such as dielectric or polarization effects [116–120] that prevent us from making quantitative predictions. Regardless, we observe qualitatively similar trends in both theory and experiment, showing that this theoretical model captures key physical behaviors in blocky polyampholyte self-coacervation.

We extend our comparison of experiment and theory to consider how blockiness τ leads to changes in self-coacervation. We plot the salt resistance ϕ_s^r as a function of the blockiness τ for both theory (Figure 9a) and experiment (Figure 9b). These data further highlight the general trend of increasing salt resistance with increasing blockiness above some τ below which no phase separation is observed. For our theoretical model, this value is roughly around $\tau = 20$, while for experiments this value is around $\tau = 15$.

We show that the relative position of the homopolyelectrolyte versus polyampholyte salt resistance depends on the particular measurement. As mentioned previously, the critical salt concentration ϕ_s^{cr} exhibits a crossover at low τ related to the interplay between translational entropy and sequence-effects. However, experiments measure the related value of salt resistance ϕ_s^r that is calculated at a defined ϕ_p; in Figure 9a we plot both ϕ_s^{cr} and ϕ_s^r, with the latter for a number of values of ϕ_p. Indeed, the crossover observed for the critical point disappears and the trend of lower salt resistance for homopolyelectrolytes compared with polyampholytes emerges at the lower values of ϕ_p that correspond with experiments.

Lastly, our experimental efforts revealed a surprising result. The polypeptides used in our experiments were synthesized using amino acids of alternating chirality to mitigate interpeptide hydrogen bond formation and subsequent β-sheet formation. [106–108] While we observed liquid-liquid phase separation

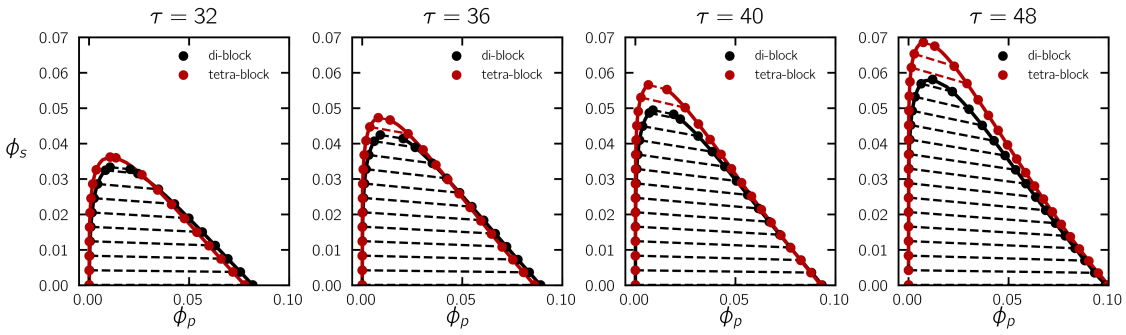

Fig. 7 Plots comparing the phase diagrams for di-block polyampholytes (black) and tetra-block polyampholytes (red) for varying values of τ.

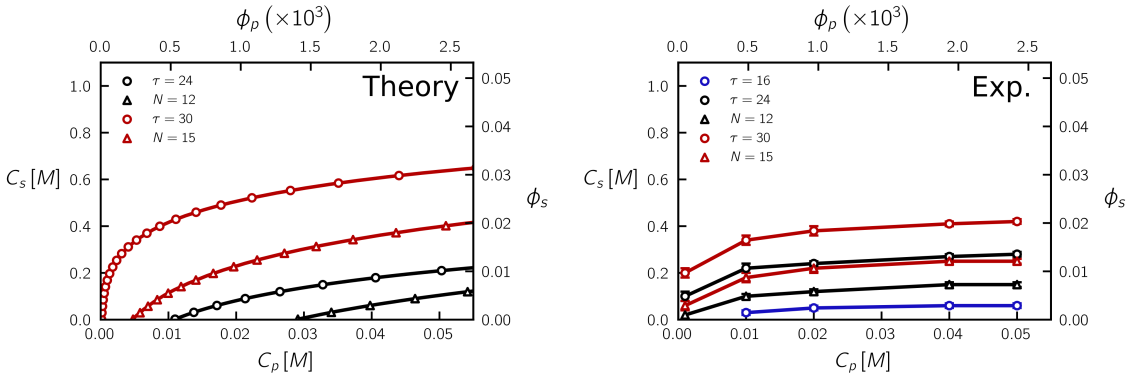

Fig. 8 Plots of the dilute branch of the binodal as a function of ϕ_s versus ϕ_p for theory (a) and experiment (b), for di-block polyampholytes with $\tau = 16, 24, 30$ (circles) and the corresponding $N_p = 12, 15$ homopolyelectrolyte coacervates (triangles). The transfer matrix theory reproduces trends observed in experiment; namely, the two-phase region increases with increasing block length (N, τ) and is higher for block polyampholytes versus homopolyelectrolytes.

for most of our samples, precipitation and β-sheet formation occurred for polyampholytes with $\tau = 48$ (Figure 10). Evidence for β-sheet formation can be seen through FTIR analysis (Figure 10), where only the $\tau = 48$ sample showed a peak at 1623 cm^{-1}, as well as an additional low-intensity peak present near 1680 cm^{-1}, which are both indicative of β-sheet formation.[106,121–123]

This unexpected β-sheet formation is similar to recent reports by Tabandeh and Leon, however it is unclear whether the mechanism is the same.[124] The work by Tabandeh and Leon looked at complexation between patterned polypeptides with different levels of hydrophobicity and attributed β-sheet formation to decreased steric clashing between D and L monomers because of the shorter side-chain length of the hydrophobic residues. However, the polymers in our system consist solely of lysine and glutamate, and show no evidence of precipitation when present as equivalent length homopolyelectrolytes. This result requires additional investigation that is beyond the scope of the current work.

5 Conclusions

We have developed a simulation-informed theoretical model for the phase behavior of polyampholytes that undergo self-coacervation, specifically in the limit where the charge density is sufficiently high that salt ion localization is a significant driver of coacervate formation. We show that the sequence, or pattern, of charges along these polyampholytes plays a large role in their ability to undergo coacervation. As the chains become more blocky, charge localization - and correspondingly the strength of coacervation - increases significantly. This increase in coacervation is similar to the effect of increasing the length of chains in homopolymer coacervation, however we show that there is a trade-off associated with the increase in number of charges per chain for equivalent polyampholyte chains and the increase in the number of charge-pattern interfaces. These charge-pattern interfaces weaken charge localization near polyampholyte chains, and thus weaken the electrostatic driving force for coacervation.

Our predicted trends are also qualitatively consistent with experimental results, including the increase in salt resistance for polyampholytes compared to corresponding homopolyelectrolytes, and an increase in the salt resistance with increasing charge blockiness. We also show that there are subtleties in how this comparison is made. In particular, the polymer concentration at which salt resistance is measured can lead to differences between the polyampholytes and equivalent homopolyelectrolytes as the competition between translational entropy and charge-pattern interface effects affects the critical point and location of the binodal.

We note that this theoretical framework uses a number of assumptions that limit the approach; most importantly, the transfer matrix theory invokes a mean-field approximation for the charges that adsorb to the test polyampholyte. This is similar to approximations made in classical polymer mean-field theories in that the polymer interactions characterizing the dilute branch of the bin-

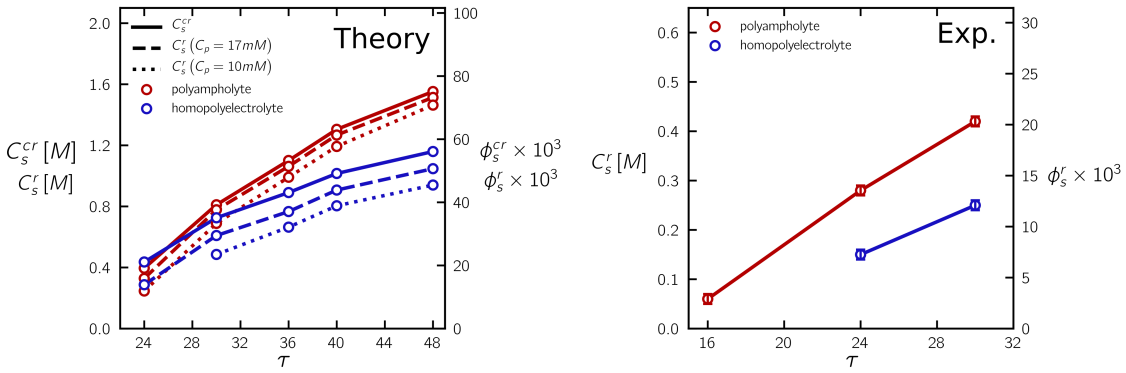

Fig. 9 Critical salt concentration ϕ_s^{cr} and salt resistance ϕ_s^r as a function of τ in theory (a) and experiment (b) for $\chi = 0.25$. In (a), we demonstrate that different measures of coacervate phase behavior result in subtly different behaviors for the block polyampholyte (pa) versus the homopolyelectrolyte (hpe) coacervates; the critical salt concentration ϕ_s^{cr} exhibits a crossover at $\tau \approx 24$, while the salt resistance ϕ_s^r shows larger differences between the two cases as the concentration ϕ_p at which they are measured is decreased. This is consistent with the experimental results in (b), which show a distinctly lower value of ϕ_s^r for the homopolyelectrolyte than the block polyampholyte coacervates.

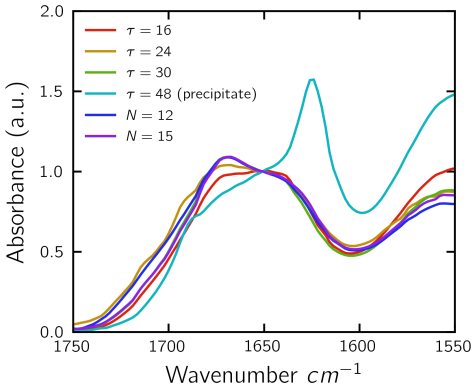

Fig. 10 FTIR of polyampholyte/homopolypeptide complexes. FTIR spectra showing the amide I region for the liquid complex coacervates and solid precipitates. All complexes showed a peak at 1564 cm^{-1} and 1673 cm^{-1}, corresponding to the carbonyl stretch of the glutamic acid and TFA counter-ion,[125] respectively. A peak at 1644 cm^{-1}, characteristic of random coil structure, was observed amongst the samples that underwent liquid-liquid phase separation. However, peaks at 1623 cm^{-1} and 1680 cm^{-1} that are characteristic of β-sheets were observed for the solid complexes formed by the $\tau = 48$ polyampholyte. The signal was normalized at 1650 cm^{-1}.

odal will not reflect the highly-correlated intra-chain interactions that are known to characterize molecular structure in the dilute supernatant phase. We also expect inaccuracies in the phase diagram at the critical point, due to the mean-field nature of the underlying polymer field theory. This assumption would only lead to quantitative deviations that would not affect qualitative trends, and could be relaxed by using more sophisticated polymer field theories or by coupling the transfer matrix formalism with spatial correlations.

We have, for this paper, focused primarily on regular polyampholyte sequences and compared with experiments using model polypeptides. This sets the foundation to consider more complicated sequences and copolymers/copolypeptides. We expect this framework to thus have implications for biologically-relevant macromolecules, such as intrinsically-disordered proteins (IDPs), which are known to undergo liquid-liquid phase separation in ways that are affected by charge monomer sequence.[9,32,46,47]

6 Acknowledgements

This material is based upon work supported by the National Science Foundation Graduate Research Fellowship Program under Grant No. DGE-1746047. We thank the Sloan Minority PhD Program as well as the University of Illinois Graduate Fellowship for additional financial support. We thank Dr. Tyler Lytle for providing valuable feedback and insight to this project.

References

1 P. E. Wright and H. Dyson, *J. Mol. Biol.*, 1999, **293**, 321–331.
2 V. N. Uversky, J. R. Gillespie and A. L. Fink, *Proteins: Struct., Funct., Bioinf.*, 2000, **41**, 415–427.
3 H. J. Dyson and P. E. Wright, *Curr. Opin. Struct. Biol.*, 2002, **12**, 54–60.
4 M.-J. Gething and J. Sambrook, *Nature*, 1992, **355**, 33.
5 C. M. Dobson, *Nature*, 2003, **426**, 884.
6 P. E. Leopold, M. Montal and J. N. Onuchic, *Proc. Natl. Acad. Sci. U. S. A.*, 1992, **89**, 8721–8725.
7 C. B. Anfinsen, E. Haber, M. Sela and F. H. White, *Proc. Natl. Acad. Sci. U. S. A.*, 1961, **47**, 1309–1314.

8 P. Romero, Z. Obradovic, X. Li, E. C. Garner, C. J. Brown and A. K. Dunker, *Proteins: Struct., Funct., Genet.*, 2001, **42**, 38–48.

9 R. K. Das and R. V. Pappu, *Proc. Natl. Acad. Sci. U. S. A.*, 2013, **110**, 13392–13397.

10 V. Receveur-Bréhot, J. M. Bourhis, V. N. Uversky, B. Canard and S. Longhi, *Proteins: Struct., Funct., Genet.*, 2006, **62**, 24–45.

11 R. W. Kriwacki, L. Hengst, L. Tennant, S. I. Reed and P. E. Wright, *Proc. Natl. Acad. Sci. U. S. A.*, 1996, **93**, 11504–11509.

12 M. Fuxreiter, I. Simon, P. Friedrich and P. Tompa, *J. Mol. Biol.*, 2004, **338**, 1015–1026.

13 P. Tompa and M. Fuxreiter, *Trends Biochem. Sci.*, 2008, **33**, 2–8.

14 M. Fuxreiter and P. Tompa, *Fuzziness*, Springer, 2012, pp. 1–14.

15 P. S. Brzovic, C. C. Heikaus, L. Kisselev, R. Vernon, E. Herbig, D. Pacheco, L. Warfield, P. Littlefield, D. Baker, R. E. Klevit *et al.*, *Mol. Cell*, 2011, **44**, 942–953.

16 R. Sharma, Z. Raduly, M. Miskei and M. Fuxreiter, *FEBS Lett.*, 2015, **589**, 2533–2542.

17 A. H. Mao, S. L. Crick, A. Vitalis, C. L. Chicoine and R. V. Pappu, *Proc. Natl. Acad. Sci. U. S. A.*, 2010, **107**, 8183–8188.

18 S. Muller-Spath, A. Soranno, V. Hirschfeld, H. Hofmann, S. Rüegger, L. Reymond, D. Nettels and B. Schuler, *Proc. Natl. Acad. Sci. U. S. A.*, 2010, **107**, 14609–14614.

19 L. M. Iakoucheva, P. Radivojac, C. J. Brown, T. R. O'Connor, J. G. Sikes, Z. Obradovic and A. K. Dunker, *Nucleic Acids Res.*, 2004, **32**, 1037–1049.

20 P. E. Wright and H. J. Dyson, *Nat. Rev. Mol. Cell Biol.*, 2015, **16**, 18–29.

21 L. M. Iakoucheva, C. J. Brown, J. D. Lawson, Z. Obradović and A. K. Dunker, *J. Mol. Biol.*, 2002, **323**, 573–584.

22 A. K. Dunker, I. Silman, V. N. Uversky and J. L. Sussman, *Curr. Opin. Struct. Biol.*, 2008, **18**, 756–764.

23 R. K. Das, Y. Huang, A. H. Phillips, R. W. Kriwacki and R. V. Pappu, *Proc. Natl. Acad. Sci. U. S. A.*, 2016, **113**, 5616–5621.

24 M. T. Wei, S. Elbaum-Garfinkle, A. S. Holehouse, C. C. H. Chen, M. Feric, C. B. Arnold, R. D. Priestley, R. V. Pappu and C. P. Brangwynne, *Nat. Chem.*, 2017, **9**, 1118–1125.

25 J. A. Toretsky and P. E. Wright, *J. Cell Biol.*, 2014, **206**, 579–588.

26 C. P. Brangwynne, P. Tompa and R. V. Pappu, *Nat. Phys.*, 2015, **11**, 899–904.

27 M. Kato, T. W. Han, S. Xie, K. Shi, X. Du, L. C. Wu, H. Mirzaei, E. J. Goldsmith, J. Longgood, J. Pei, N. V. Grishin, D. E. Frantz, J. W. Schneider, S. Chen, L. Li, M. R. Sawaya, D. Eisenberg, R. Tycko and S. L. McKnight, *Cell*, 2012, **149**, 753–767.

28 J. T. Wang, J. Smith, B.-C. Chen, H. Schmidt, D. Rasoloson, A. Paix, B. G. Lambrus, D. Calidas, E. Betzig and G. Seydoux, *eLife*, 2014, **3**, 1–23.

29 S. Elbaum-Garfinkle, Y. Kim, K. Szczepaniak, C. C.-H. Chen, C. R. Eckmann, S. Myong and C. P. Brangwynne, *Proc. Natl. Acad. Sci. U. S. A.*, 2015, **112**, 7189–7194.

30 P. Li, S. Banjade, H. C. Cheng, S. Kim, B. Chen, L. Guo, M. Llaguno, J. V. Hollingsworth, D. S. King, S. F. Banani, P. S. Russo, Q. X. Jiang, B. T. Nixon and M. K. Rosen, *Nature*, 2012, **483**, 336–340.

31 S. Alberti, A. Gladfelter and T. Mittag, *Cell*, 2019, **176**, 419–434.

32 T. J. Nott, E. Petsalaki, P. Farber, D. Jervis, E. Fussner, A. Plochowietz, T. D. Craggs, D. P. Bazett-Jones, T. Pawson, J. D. Forman-Kay and A. J. Baldwin, *Mol. Cell*, 2015, **57**, 936–947.

33 S. L. Perry, *Curr. Opin. Colloid Interface Sci.*, 2019, **39**, 86–97.

34 J. Berry, C. P. Brangwynne and M. Haataja, *Rep. Prog. Phys.*, 2018, **81**, 046601.

35 C. P. Brangwynne, T. J. Mitchison and A. A. Hyman, *Proc. Natl. Acad. Sci. U. S. A.*, 2011, **108**, 4334–4339.

36 C. P. Brangwynne, C. R. Eckmann, D. S. Courson, A. Rybarska, C. Hoege, J. Gharakhani, F. Jülicher and A. A. Hyman, *Science*, 2009, **324**, 1729–1732.

37 M. Feric, N. Vaidya, T. S. Harmon, D. M. Mitrea, L. Zhu, T. M. Richardson, R. W. Kriwacki, R. V. Pappu and C. P. Brangwynne, *Cell*, 2016, **165**, 1686–1697.

38 C. F. Lee, C. P. Brangwynne, J. Gharakahani, A. A. Hyman and F. Jülicher, *Phys. Rev. Lett.*, 2013, **111**, 088101.

39 Y. Shin and C. P. Brangwynne, *Science*, 2017, **357**, eaaf4382.

40 S. C. Weber and C. P. Brangwynne, *Cell*, 2012, **149**, 1188–1191.

41 L. Zhu and C. P. Brangwynne, *Curr. Opin. Cell Biol.*, 2015, **34**, 23–30.

42 S. F. Banani, H. O. Lee, A. A. Hyman and M. K. Rosen, *Nat. Rev. Mol. Cell Biol.*, 2017, **18**, 285–298.

43 A. A. Hyman, C. A. Weber and F. Jülicher, *Annu. Rev. Cell Dev. Biol.*, 2014, **40**, 39–58.

44 A. A. Hyman and K. Simons, *Science*, 2012, **337**, 1047–1049.

45 P. Li, S. Banjade, H.-C. Cheng, S. Kim, B. Chen, L. Guo, M. Llaguno, J. V. Hollingsworth, D. S. King, S. F. Banani, P. S. Russo, Q.-X. Jiang, B. T. Nixon and M. K. Rosen, *Nature*, 2012, **483**, 336–340.

46 F. G. Quiroz and A. Chilkoti, *Nat. Mater.*, 2015, **14**, 1164–1171.

47 C. W. Pak, M. Kosno, A. S. Holehouse, S. B. Padrick, A. Mittal, R. Ali, A. A. Yunus, D. R. Liu, R. V. Pappu and M. K. Rosen, *Mol. Cell*, 2016, **63**, 72–85.

48 W. M. Aumiller and C. D. Keating, *Nat. Chem.*, 2016, **8**, 129–137.

49 P. G. Higgs and J. F. Joanny, *J. Chem. Phys.*, 1991, **94**, 1543–1554.

50 Andrey V. Dobrynin and Michael Rubinstein, *J. Phys. II France*, 1995, **5**, 677–695.

51 L. Sawle and K. Ghosh, *J. Chem. Phys.*, 2015, **143**, 085101.

52 T. Firman and K. Ghosh, *J. Chem. Phys.*, 2018, **148**, 123305.

53 Y. Kantor, H. Li and M. Kardar, *Phys. Rev. Lett.*, 1992, **69**, 61–64.

54 B. Xu, L. Huang and H. Liang, *J. Chem. Phys.*, 2004, **121**, 7494–7500.

55 H. S. Samanta, D. Chakraborty and D. Thirumalai, *J. Chem. Phys.*, 2018, **149**, 163323.

56 D. Srivastava and M. Muthukumar, *Macromolecules*, 1996, **29**, 2324–2326.

57 J. Jiang, J. Feng, H. Liu and Y. Hu, *J. Chem. Phys.*, 2006, **124**, 144908.

58 D. W. Cheong and A. Z. Panagiotopoulos, *Mol. Phys.*, 2005, **103**, 3031–3044.

59 S. Das, A. Eisen, Y. H. Lin and H. S. Chan, *J. Phys. Chem. B*, 2018, **122**, 5418–5431.

60 Y. H. Lin, J. D. Forman-Kay and H. S. Chan, *Phys. Rev. Lett.*, 2016, **117**, 1–6.

61 Y. H. Lin, J. Song, J. D. Forman-Kay and H. S. Chan, *J. Mol. Liq.*, 2017, **228**, 176–193.

62 S. P. O. Danielsen, J. McCarty, J.-E. Shea, K. T. Delaney and G. H. Fredrickson, *Proc. Natl. Acad. Sci. U. S. A.*, 2019, 8224–8232.

63 K. T. Delaney and G. H. Fredrickson, *J. Chem. Phys.*, 2017, **146**, 224902.

64 J. McCarty, K. T. Delaney, S. P. O. Danielsen, G. H. Fredrickson and J.-E. Shea, *J. Phys. Chem. Lett.*, 2019, **10**, 1644–1652.

65 A. L. Patterson, S. P. O. Danielsen, B. Yu, E. C. Davidson, G. H. Fredrickson and R. A. Segalman, *Macromolecules*, 2019, **52**, 1277–1286.

66 D. A. McQuarrie, *Statistical Mechanics*, HarperCollins Publishing, Inc., New York, 1976.

67 J. T. G. Overbeek and M. Voorn, *J. Cell. Comp. Physiol.*, 1957, **49**, 7–26.

68 I. Michaeli, J. T. G. Overbeek and M. Voorn, *J. Polym. Sci.*, 1957, **23**, 443–450.

69 R. A. Riggleman, R. Kumar and G. H. Fredrickson, *J. Chem. Phys.*, 2012, **136**, 024903.

70 J. Lee, Y. O. Popov and G. H. Fredrickson, *J. Chem. Phys.*, 2008, **128**, 224908.

71 D. J. Audus, J. D. Gopez, D. V. Krogstad, N. A. Lynd, E. J. Kramer, C. J. Hawker and G. H. Fredrickson, *Soft Matter*, 2015, **11**, 1214–1225.

72 J. Qin and J. J. de Pablo, *Macromolecules*, 2016, **49**, 8789–8800.

73 A. Kudlay, A. V. Ermoshkin and M. Olvera de La Cruz, *Macromolecules*, 2004, **37**, 9231–9241.

74 A. Kudlay and M. Olvera de la Cruz, *J. Chem. Phys.*, 2004, **120**, 404–412.

75 M. Castelnovo and J.-F. Joanny, *Eur. Phys. J. E: Soft Matter Biol. Phys.*, 2001, **6**, 377–386.

76 C. E. Sing, *Adv. Colloid Interface Sci.*, 2017, **239**, 2–16.

77 E. Spruijt, A. H. Westphal, J. W. Borst, M. A. Cohen Stuart and J. van der Gucht, *Macromolecules*, 2010, **43**, 6476–6484.

78 D. Priftis and M. Tirrell, *Soft Matter*, 2012, **8**, 9396–9405.

79 S. Perry, Y. Li, D. Priftis, L. Leon and M. Tirrell, *Polymers*, 2014, **6**, 1756–1772.

80 Z. Ou and M. Muthukumar, *J. Chem. Phys.*, 2006, **124**, 154902.

81 S. Liu and M. Muthukumar, *J. Chem. Phys.*, 2002, **116**, 9975–9982.

82 R. S. Dias, P. Linse and A. A. C. C. Pais, *J. Comput. Chem.*, 2011, **32**, 2697–2707.

83 J. Jeon and A. V. Dobrynin, *J. Phys. Chem. B*, 2006, **110**, 24652–24665.

84 V. S. Rathee, H. Sidky, B. J. Sikora and J. K. Whitmer, *J. Am. Chem. Soc.*, 2018, **140**, 15319–15328.

85 V. S. Rathee, A. J. Zervoudakis, H. Sidky, B. J. Sikora and J. K. Whitmer, *J. Chem. Phys.*, 2018, **148**, 114901.

86 S. L. Perry and C. E. Sing, *Macromolecules*, 2015, **48**, 5040–5053.

87 P. Zhang, N. M. Alsaifi, J. Wu and Z.-G. Wang, *J. Chem. Phys.*, 2018, **149**, 163303.

88 P. Zhang, K. Shen, N. M. Alsaifi and Z.-G. Wang, *Macromolecules*, 2018, **51**, 5586–5593.

89 Z. Wang and M. Rubinstein, *Macromolecules*, 2006, **39**, 5897–5912.

90 M. Rubinstein, Q. Liao and S. Panyukov, *Macromolecules*, 2018, **51**, 9572–9588.

91 A. M. Rumyantsev, E. Y. Kramarenko and O. V. Borisov, *Macromolecules*, 2018, **51**, 6587–6601.

92 A. M. Rumyantsev, E. B. Zhulina and O. V. Borisov, *Macromolecules*, 2018, **51**, 3788–3801.

93 G. S. Manning, *J. Chem. Phys.*, 1969, **51**, 924–933.

94 S. Friedowitz, A. Salehi, R. G. Larson and J. Qin, *J. Chem. Phys.*, 2018, **149**, 163335.

95 S. Adhikari, M. A. Leaf and M. Muthukumar, *J. Chem. Phys.*, 2018, **149**, 163308.

96 T. K. Lytle and C. E. Sing, *Soft Matter*, 2017, **13**, 7001–7012.

97 T. K. Lytle and C. E. Sing, *Mol. Syst. Des. Eng.*, 2018, **3**, 183–196.

98 T. K. Lytle, A. J. Salazar and C. E. Sing, *J. Chem. Phys.*, 2018, **149**, 163315.

99 T. K. Lytle, L.-W. Chang, N. Markiewicz, S. L. Perry and C. E. Sing, *ACS Cent. Sci.*, 2019, **5**, 709–718.

100 B. M. Johnston, C. W. Johnston, R. A. Letteri, T. K. Lytle, C. E. Sing, T. Emrick and S. L. Perry, *Org. Biomol. Chem.*, 2017, **15**, 7630–7642.

101 G. M. C. Ong and C. E. Sing, *Soft Matter*, 2019, **15**, 5116–5127.

102 S. P. O. Danielsen, J. McCarty, J.-E. Shea, K. Delaney and G. Fredrickson, *J. Chem. Phys.*, 2019, **151**, 034904.

103 M. Radhakrishna, K. Basu, Y. Liu, R. Shamsi, S. L. Perry and C. E. Sing, *Macromolecules*, 2017, **50**, 3030–3037.

104 L. W. Chang, T. K. Lytle, M. Radhakrishna, J. J. Madinya, J. Vélez, C. E. Sing and S. L. Perry, *Nat. Commun.*, 2017, **8**, 1273.

105 M. Amblard, J. A. Fehrentz, J. Martinez and Subra, *Mol. Biotechnol.*, 2006, **33**, 239–254.

106 S. L. Perry, L. Leon, K. Q. Hoffmann, M. J. Kade, D. Priftis,

K. A. Black, D. Wong, R. A. Klein, C. F. Pierce III, K. O. Margossian, J. K. Whitmer, J. Qin, J. J. de Pablo and M. Tirrell, *Nat. Commun.*, 2015, **6**, 6052.

107 K. Q. Hoffmann, S. L. Perry, L. Leon, D. Priftis, M. Tirrell and J. J. de Pablo, *Soft Matter*, 2015, **11**, 1525–1538.

108 N. M. Pacalin, L. Leon and M. Tirrell, *Eur. Phys. J. Special Topics*, 2016, **225**, 1805–1815.

109 Y. Liu, B. Monami, H. H. Winter and S. L. Perry, *Soft Matter*, 2017, **13**, 7332–7340.

110 L. Li, S. Srivastava, M. Andreev, A. B. Marciel, J. J. de Pablo and M. V. Tirrell, *Macromolecules*, 2018, **51**, 2988–2995.

111 P. Zhang, K. Shen, N. M. Alsaifi and Z.-G. Wang, *Macromolecules*, 2018, **51**, 5586–5593.

112 E. Sokolova, E. Spruijt, M. M. K. Hansen, E. Dubuc, J. Groen, V. Chokkalingam, A. P. H. A. Heus and W. T. S. Huck, *Proc. Natl. Acad. Sci. U. S. A.*, 2013, **110**, 11692–11697.

113 J. Qin, D. Priftis, R. Farina, S. L. Perry, L. Leon, J. Whitmer, K. Hoffmann, M. Tirrell and J. J. de Pablo, *ACS Macro Letters*, 2014, **6**, 565–568.

114 A. Salehi and R. G. Larson, *Macromolecules*, 2016, **49**, 9706–9719.

115 V. Y. Borue and I. Y. Erukhimovich, *Macromolecules*, 1990, **23**, 3625–3632.

116 X. Duan and I. Nakamura, *Soft Matter*, 2015, **11**, 3566–3571.

117 A. Levy, D. Andelman and H. Orland, *Phys. Rev. Lett.*, 2012, **108**, 227801.

118 R. Kumar and G. H. Fredrickson, *J. Chem. Phys.*, 2009, **131**, 104901.

119 M. Andreev, J. J. de Pablo, A. Chremos and J. F. Douglas, *J. Phys. Chem. B*, 2018, **122**, 4029–4034.

120 J. Lou, S. Friedowitz, J. Qin and Y. Xia, *ACS Cent. Sci.*, 2019, **5**, 549–557.

121 W. Dzwolak, R. Ravindra, C. Nicolini, R. Jansen and R. Winter, *J. Am. Chem. Soc.*, 2004, **126**, 3762–3768.

122 M. Fandrich and C. M. Dobson, *EMBO J*, 2002, **21**, 5682–5690.

123 C. R. Baiz and M. R. A. Tokmakoff, *Ultrafast Infrared Vibrational Spectroscopy*, CRC Press, 2012, pp. 5682–5690.

124 S. Tabandeh and L. Leon, *Molecules*, 2019, **24**, 868.

125 K. Janek, J. Behlke, J. Zipper, H. Fabian, Y. Georgalis, M. Beyermann, M. Bienert and E. Krause, *Biochemistry*, 1999, **38**, 8246–8252.